HIGHER-ORDER FDTD METHODS FOR LARGE PROBLEMS

Charles W. Manry Jr, Shira L. Broschat, and John B. Schneider *

Abstract

The Finite-Difference Time-Domain (FDTD) algorithm provides a simple and efficient means of solving Maxwell's equations for a wide variety of problems. In Yee's uniform grid FDTD algorithm the derivatives in Maxwell's curl equations are replaced by central difference approximations. Unfortunately, numerical dispersion and grid anisotropy are inherent to FDTD methods. For large computational domains, e.g., ones that have at least one dimension forty wavelengths or larger, phase errors from dispersion and grid anisotropy in the Yee algorithm (YA) can be significant unless a small spatial discretization is used. For such problems, the amount of data that must be stored and calculated at each iteration can lead to prohibitive memory requirements and high computational cost. To decrease the expense of FDTD simulations for large scattering problems two higher-order methods have been derived and are reported here. One method is second-order in time and fourth-order in space (2-4); the other is second-order in time and sixth-order in space (2-6). Both methods decrease grid anisotropy and have less dispersion than the YA at a set discretization. Also, both permit a coarser discretization than the YA for a given error bound.

To compare the accuracy of the YA and higher-order methods both transient and CW simulations have been performed at a set discretization. In general, it has been found that the higher-order methods are more accurate than the YA due to the reduced grid anisotropy and dispersion. However, the higher-order methods are not as accurate as the YA for the simulation of surface waves. This is attributed to the larger spatial stencil used in calculating the fields for the higher-order methods. More research is needed to examine the accuracy of higher-order methods at material boundaries.

I. Introduction

Yee's uniform grid Finite-Difference Time-Domain (FDTD) algorithm provides a direct solution to Maxwell's time-dependent curl equations and permits the analysis of both transient and steady-state problems [1]. In this algorithm, both time and space are discretized, and second-order central-difference approximations of derivatives are used to obtain a set of simple equations which yield future field values based on past and present field quantities. The equations are numerically exact, i.e., no physical assumptions are made regarding energy propagation and interaction with scattering materials. Numerical error is controlled by the discretization size, and computational and storage requirements are proportional to the electrical size of the problem [2]. However, the algorithm is inherently dispersive and anisotropic [2]. For large problems, forty wavelengths or larger, errors from dispersion and anisotropy are significant (here a phase difference greater than $\pi/8$ is considered significant) unless the spatial discretization is very small. This can lead to prohibitive memory requirements and high computational cost.

To decrease the resources required to perform large FDTD simulations higher-order FDTD methods can be used. By improving the accuracy of the approximations for the spatial derivatives in Maxwell's curl equations, numerical dispersion and grid anisotropy are reduced. The two methods presented here are second-order in time and fourth-order in space (2-4) and second-order in time and sixth-order in space (2-6). Both methods are less dispersive than the Yee algorithm (YA) and permit larger spatial and temporal discretizations which, in turn, allow faster computation time and the storage of less data. For a given discretization the higher-order methods provide a more accurate simulation than the YA for the test cases examined.

In this paper 2-4 and 2-6 algorithms are derived and suitable boundary conditions are developed. In addition, the results from simulations using the YA, 2-4, and 2-6 methods are examined and compared. The simulations are done using a moderate spatial discretization and demonstrate the improvement in accuracy for the higher-order methods. First, a two-dimensional transient pulse in free-space is simulated to demonstrate the effect of grid anisotropy and dispersion in the three algorithms. Next a harmonic scattering problem is considered to examine the accuracy of the methods. The magnitude and phase of the field scattered from a large cylinder are measured and compared to results found using a moment method solution. In general, because of reduced dispersion, the higher-order methods are more accurate than the YA.

*The authors are with the School of Electrical Engineering and Computer Science Washington State University, Pullman, WA 99164-2752

However, the YA is more accurate in magnitude near the shadow boundary. It is found that the higher-order methods are not as accurate as the YA for the simulation of guided waves due to the wider spatial stencil used to calculate the fields. Nevertheless, the higher-order methods provide a more accurate simulation tool than the YA for the study of large scattering problems at moderate discretizations (10-20 PPW).

II. The Yee Algorithm

We will consider only two-dimensional, TM problems although the higher-order algorithms can be extended easily to three-dimensional problems and other polarizations. In the YA, second-order central-difference equations are used to approximate Maxwell's curl equations. Space and time are discretized to ensure stability [2, 3]. The resulting equations for lossless media are

$$\begin{aligned} E_z^{n+1}(i,j) &= E_z^n(i,j) \\ &+ \frac{\Delta t}{\epsilon(i,j)\Delta x}\left(H_y^{n+\frac{1}{2}}(i+\tfrac{1}{2},j) - H_y^{n+\frac{1}{2}}(i-\tfrac{1}{2},j)\right) \\ &- \frac{\Delta t}{\epsilon(i,j)\Delta y}\left(H_x^{n+\frac{1}{2}}(i,j+\tfrac{1}{2}) - H_x^{n+\frac{1}{2}}(i,j-\tfrac{1}{2})\right) \end{aligned} \quad (1)$$

$$\begin{aligned} H_y^{n+\frac{1}{2}}(i+\tfrac{1}{2},j) &= H_y^{n-\frac{1}{2}}(i+\tfrac{1}{2},j) \\ &+ \frac{\Delta t}{\mu(i+\frac{1}{2},j)\Delta x}\left(E_z^n(i+1,j) - E_z^n(i,j)\right) \end{aligned} \quad (2)$$

$$\begin{aligned} H_x^{n+\frac{1}{2}}(i,j+\tfrac{1}{2}) &= H_x^{n-\frac{1}{2}}(i,j+\tfrac{1}{2}) \\ &- \frac{\Delta t}{\mu(i,j+\frac{1}{2})\Delta y}\left(E_z^n(i,j+1) - E_z^n(i,j)\right) \end{aligned} \quad (3)$$

where $E_z^n(i,j) = E_z(i\Delta x,\ j\Delta y,\ n\Delta t)$, $\epsilon(i,j) = \epsilon(i\Delta x,\ j\Delta y)$, $\mu(i+\frac{1}{2},j) = \mu([i+\frac{1}{2}]\Delta x,\ j\Delta y)$, $\mu(i,j+\frac{1}{2}) = \mu(i\Delta x,\ [j+\frac{1}{2}]\Delta y)$, Δx and Δy are the spatial discretizations, and Δt is the temporal discretization. For our work, $\Delta x = \Delta y = h = \lambda_{\min}/\mathrm{PPW}$, where $\lambda_{\min} = c_{\min}/f$ is the smallest wavelength in the scattering problem for a given frequency, f. Finally, $\Delta t = h/2c_{\max}$ to satisfy stability requirements where $c_{\max}$ and $c_{\min}$ are the fastest and slowest medium velocities for the problem geometry, respectively. Appendix A provides a stability analysis for the YA as well as the higher-order methods.

To examine the amount of dispersion in the YA, the normalized numerical phase velocity is plotted in Fig. 1 as a function of the PPW discretization (higher-order methods are also presented in Figs. 1-3 and are discussed in the next section). Another way to examine dispersion is to calculate the phase error per wavelength due to dispersion; this is plotted in Fig. 2 (see Appendix B for details concerning the calculation of dispersion curves). In both figures the solid-circle line pertains to a plane wave traveling at $0°$ with respect to the grid lines while the hollow-circle line is for a plane wave traveling at $45°$. These cases represent minimum and maximum propagation angles with respect to the grid lines. Note that in Fig. 1 both the YA dispersion curves are always less than unity, the ideal case, and both curves decrease rapidly for PPW less than 10. Thus, higher frequencies travel more slowly than lower frequencies, causing broadening and distortion of a propagating pulse. Furthermore, the amount of dispersion depends on the direction of propagation. Figure 2 also indicates the amount of grid anisotropy for the YA in that the phase error per wavelength is approximately two to four times larger for the plane wave traveling at $0°$ than the plane wave traveling at $45°$.

To gain a better measure of the effect of grid anisotropy, the phase difference per wavelength between a plane wave propagating at $0°$ and one propagating at $45°$ with respect to the grid lines is plotted in Fig. 3. The distance required to obtain a phase difference of $\pi/8$ was calculated using 10, 20, and 40 PPW. These results are presented in Table 1. Dispersion and grid anisotropy can be decreased by increasing the PPW; however, a high PPW value coupled with a large computational domain is costly. The memory required for a $n\lambda$-by-$m\lambda$ problem is given by $nm \cdot 58 \cdot (\mathrm{PPW})^2$ bytes assuming double precision (8 byte) variables for the field components and material parameters. The memory requirements for a $n\lambda$-by-$m\lambda$ problem discretized at 10, 20, and 40 PPW are given in Table 1. Note that at 40 PPW, where grid anisotropy and dispersion are relatively small, the requirement is $nm \cdot 87.5$ KB. As an example, for a 40λ-by-40λ problem the memory required is 141.6 MB.

Since the memory requirement is $O(\mathrm{PPW}^2)$, it can be greatly reduced by decreasing the PPW. Additionally, the overall computation cost can be decreased since the number of operations needed to simulate the propagation of a pulse across the computational domain is $O(\mathrm{PPW}^3)$. Thus, a method that has acceptable grid anisotropy and dispersion at moderate PPW values (10 to 20 PPW) is needed to solve large problems more efficiently.

III. Higher-Order Techniques

One way to minimize numerical dispersion is to improve the accuracy of the difference equations used to approximate Maxwell's curl equations. Previous authors have derived fourth-order approximations using additional terms of a Taylor series expansion [4]-[9]. Alternatively, the fields can be approximated by four- or six-point Lagrange interpolating polynomials. The derivatives of these Lagrange polynomials are then taken to obtain fourth- or

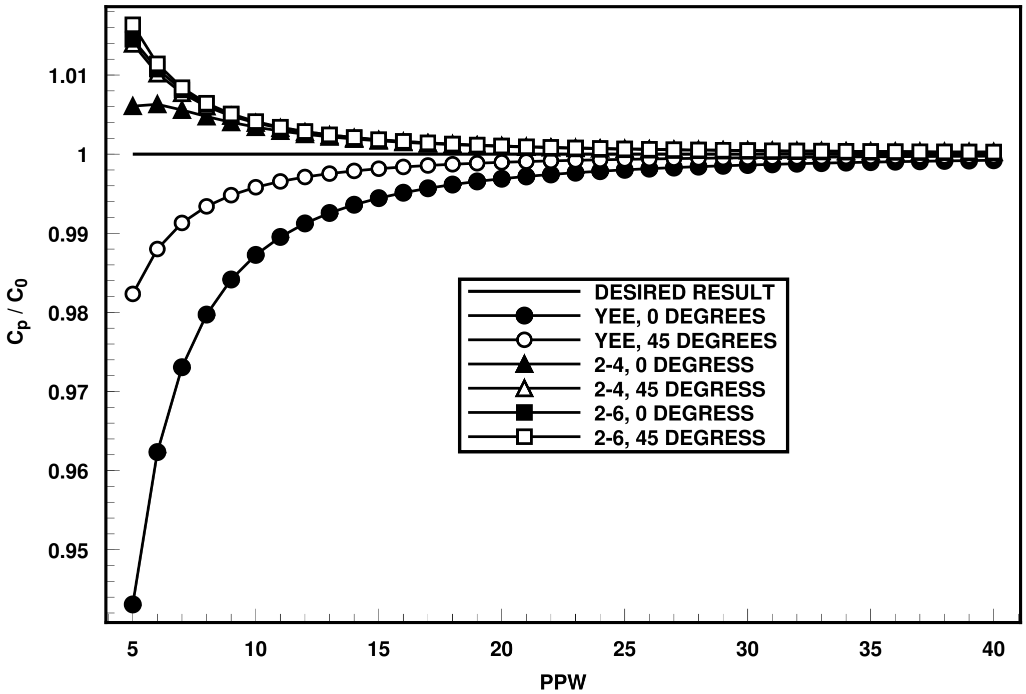

Figure 1: Normalized dispersion curves for the YA, 2-4 method, and the 2-6 method for a plane wave traveling at 0° and 45° with respect to the grid lines versus points per wavelength (PPW) discretization.

sixth-order approximations, respectively. The final difference equations obtained from a Taylor series expansion or using Lagrange polynomials are identical. The four-point Lagrange interpolating polynomial, along the x axis, for the electric field is [10]

$$\begin{aligned} E_z^n(i+p,j) &= -\frac{p(p-1)(p-2)}{6}E_z^n(i-1,j) \\ &+ \frac{(p^2-1)(p-2)}{2}E_z^n(i,j) \\ &- \frac{p(p+1)(p-2)}{2}E_z^n(i+1,j) \\ &+ \frac{p(p^2-1)}{6}E_z^n(i+2,j) \\ &+O(h^4) \end{aligned} \tag{4}$$

Taking the derivative of (4) with respect to p and evaluating at $x=(i+1/2)h$, (i.e., $p=1/2$) gives

$$\begin{aligned} \frac{\partial}{\partial x}E_z^n(i+1/2,j) &= \tfrac{1}{24h}\left[E_z(i-1,j) - 27E_z(i,j)\right. \\ &\left.+ 27E_z(i+1,j) - E_z(i+2h,j)\right] + O(h^4) \end{aligned} \tag{5}$$

Similarly, the sixth-order approximation is given by

$$\begin{aligned} \frac{\partial}{\partial x}E_z^n(i+1/2,j) &= \tfrac{1}{1920h}\left[-9E_z^n(i-2,j)\right. \\ &+ 125E_z^n(i-1,j) - 2250E_z^n(i,j) + 2250E_z^n(i+1,j) \\ &\left.- 125E_z^n(i+2,j) + 9E_z^n(i+3,j)\right] + O(h^6) \end{aligned} \tag{6}$$

The derivatives with respect to y are found using the same approach.

This technique can be applied to temporal as well as to spatial differencing [9], but application to the temporal derivatives requires storage of more temporal values than Yee's method. Fang has developed a fourth-order in time and space algorithm that does not require additional temporal values but requires additional spatial field values [8]. Since one of our goals is to minimize memory requirements so that large problems can be simulated, the higher-order differencing methods are applied only to spatial derivatives. This yields a second-order in time and fourth-order in space or a second-order in time and sixth-order in space set of differencing equations. For example, the equation for updating the electric field in the 2-4 (lossless) method is

$$\begin{aligned} E_z^{n+1}(i,j) &= E_z^n(i,j) + \Delta t/(24\epsilon(i,j)h)\cdot \\ &\Big(H_y^{n+\frac{1}{2}}(i-\tfrac{3}{2},j) - 27H_y^{n+\frac{1}{2}}(i-\tfrac{1}{2},j) \\ &+ 27H_y^{n+\frac{1}{2}}(i+\tfrac{1}{2},j) - H_y^{n+\frac{1}{2}}(i+\tfrac{3}{2},j) \\ &- H_x^{n+\frac{1}{2}}(i,j-\tfrac{3}{2}) + 27H_x^{n+\frac{1}{2}}(i,j-\tfrac{1}{2}) \\ &- 27H_x^{n+\frac{1}{2}}(i,j+\tfrac{1}{2}) + H_x^{n+\frac{1}{2}}(i,j+\tfrac{3}{2})\Big) \end{aligned} \tag{7}$$

Stability requirements are more stringent for the higher-order methods. The stability requirement (two-

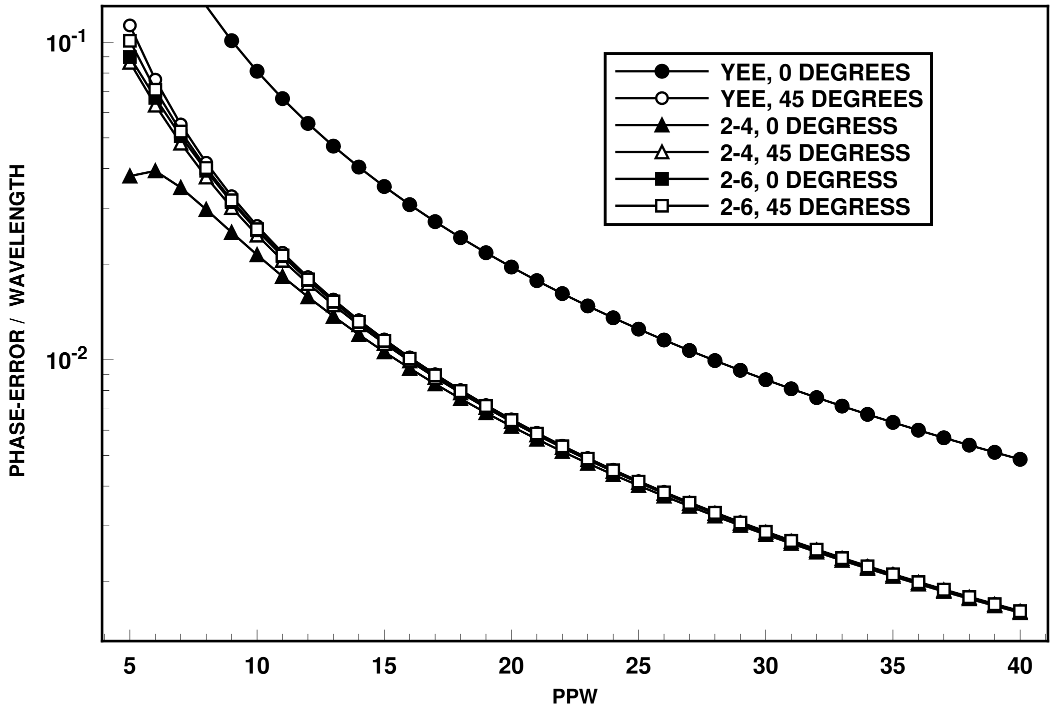

Figure 2: Phase error per wavelength curves for the YA, 2-4 and 2-6 methods for a plane wave traveling at 0° and 45° with respect to the grid lines versus points per wavelength (PPW) discretization.

dimensional) for the YA is $\Delta t \leq h/\sqrt{2}c_{\max}$. For the 2-4 method the requirement is $\Delta t \leq \frac{6}{7}h/\sqrt{2}c_{\max}$, while for the 2-6 method it is $\Delta t \leq \frac{120}{149}h/\sqrt{2}c_{\max}$. By setting $\Delta t = h/2c_{\max}$, stability is ensured for all the methods examined in this paper. Appendix A presents a stability analysis for the higher-order methods.

The 2-4 and 2-6 dispersion curves are plotted in Fig. 1 and the phase errors per wavelength are plotted in Fig. 2 (Appendix B presents the relevant equations). Note that the dispersion curves in Fig. 1 are above unity for all PPW values and that the variation between the 0° and 45° curves is much less than in the YA. For the 2-4 method the 0° and 45° curves do not differ significantly until below approximately 12 PPW while the 2-6 curves do not differ appreciably until below approximately 8 PPW. Also, the dispersion curves for the higher-order methods are flatter than those of the YA. Thus, the 2-4 and 2-6 methods will cause less pulse broadening and distortion than the YA. In Fig. 2 the phase errors for the 0° and 45° curves do not differ significantly and are approximately the same as the 45° curve for the YA. Note in Fig. 2 that the phase errors for the 2-4 and 2-6 methods are similar, but error associated with the 2-6 is slightly larger.

The results plotted in Figs. 1 and 2 are too similar to gauge how the higher-order methods affect anisotropy. To demonstrate the reduction in anisotropy, the phase error between a plane wave propagating at 0° and 45° with respect to the grid lines is plotted in Fig. 3. It can be seen that the higher-order methods decrease this error by orders of magnitude compared to the YA. The distance required to accumulate a phase difference of $\pi/8$ is presented in Table 1 for the higher-order methods. As reported previously [5]-[11], the higher-order methods provide a reduction in anisotropy at all PPW values.

With improved grid anisotropy comes a higher computational cost at each field point. For a two-dimensional problem, the number of floating point operations needed for a set of field points (E_z, H_x, H_y) is 12 for the YA, 36 for the 2-4 method, and 52 for the 2-6 method. Although the higher-order methods are more expensive per point, a smaller PPW value can be used than for the YA. Using the higher-order techniques, the lower bound on the PPW may be dictated by the physical complexity of the scatterer rather than the need to control dispersion and anisotropy.

Shlager *et al.* provide an excellent cost analysis of various higher-order FDTD methods [11]. Once the PPW is known, the memory requirements and floating point operating cost for each method can be calculated. Petropoulos derives a formula for determining the PPW for a given dispersion error for both the YA and the 2-4 method [12]. As Shlager *et al.* and Petropoulos state, for a given dispersion error the higher-order methods require less computer resources due to the smaller discretization required.

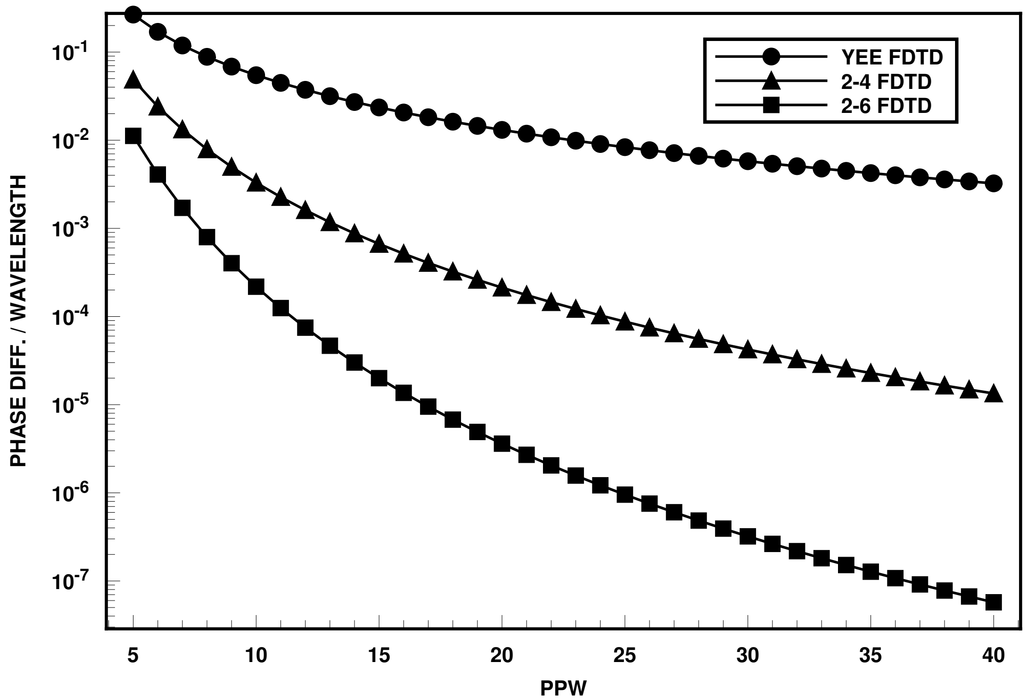

Figure 3: Phase difference between plane wave traveling at 0° and 45° with respect to the grid lines per wavelength curves for the YA, 2-4 and 2-6 methods versus points per wavelength (PPW) discretization.

PPW	YA	2-4	2-6	Memory
10	7.18λ	119.13λ	1801.95λ	$nm \cdot 5.47$ KB
20	29.98λ	1846.54λ	108666.0λ	$nm \cdot 21.86$ KB
40	121.17λ	29288.3λ	$6.85107 \times 10^6\lambda$	$nm \cdot 87.50$ KB

Table 1: Distance to produce $\pi/8$ phase error due to grid anisotropy and the required memory for a $n\lambda$-by-$m\lambda$ problem discretized at a given points per wavelength (PPW) value.

However, dispersion analysis only predicts errors in homogeneous regions. It cannot account for errors due to stair-step approximations of material boundaries. It also does not account for errors at material boundaries caused by the use of increased spatial stencils used in approximating the spatial derivatives.

In Sections 6 and 7, the accuracy of the YA, 2-4 , and 2-6 methods are compared using a free-space transient problem and scattering from a large, weakly-scattering object. In these comparisons, the PPW for each method is the same. Before examining these results the boundary conditions for the higher-order methods are covered.

IV. Absorbing Boundary Conditions

For points close to the edge of the computational grid, higher-order methods require information exterior to the computational domain. In an attempt to circumvent this problem, different FDTD algorithms were layered near the boundary. At the boundary the YA was used with a second-order, one-way wave equation operator absorbing boundary condition [13]-[15]; then the 2-4 method was used for the next set of internal points. Finally, either the 2-4 or the 2-6 algorithm was used for the remaining internal points. This approach failed because of the impedance mismatches due to the different dispersive behavior for each of the methods. A wave traveling between the 2-6, 2-4, and the YA regions is partially reflected (as if material discontinuities were present). To solve this problem Levander added a telegraphy region [16], which requires the use of an additional layer of grid points and, consequently, additional memory and computations. Another approach is to use a combination of ABCs. This approach is successful for very short transient pulses but is unstable for CW input. Small reflections from the outermost layer make the internal layers unstable.

An acceptable solution was obtained using an image based boundary method [18]. An image of the fields internal to the grid was used to find the fields outside the computational grid. At the boundary both the original internal waves and the external image waves are absorbed using the equation of images. At the right boundary [18]

$$\left(\frac{\partial^2}{c_0^2\partial t^2} - \nabla^2\right) E_z + 2\delta(x - X_b)\cdot\mathcal{B}[E_z(x = X_b)] = 0 \quad (8)$$

where c_0 is the speed of propagation in the medium, X_b is the position of the right boundary, $\delta(x - X_b)$ is the Dirac delta function, and $\mathcal{B}[E_z(x = X_b)]$ is an absorbing boundary operator.

Different absorbing boundary condition operators were examined with the image boundary method [13]-[17]. The Liao operator [17] was found to be unstable for both transient and CW inputs. Mei and Fang's superabsorbing approach was briefly examined for use with the image boundary method but was not implemented due to difficulties in combining their technique with the image method [19]. The operator found to work best was the second-order, one-way wave equation operator [13]-[15] which is given by

$$\mathcal{B}[E_z(x = X_b)] = \left(\frac{1}{c_0}\frac{\partial^2}{\partial t\partial x} + \frac{1}{c_0^2}\frac{\partial^2}{\partial t^2} - \alpha\frac{\partial^2}{\partial y^2}\right) E_z(x = X_b) \quad (9)$$

where α is the absorbing boundary condition coefficient that controls the amount of absorption at different incident angles. The second-order partial derivative terms are difficult to implement in a leap-frog time differencing scheme. To remove these terms, (9) is integrated with respect to time and Maxwell's equations for the TM-mode are used [20]. Since $\partial E_z(x = X_b)/\partial x = 0$ because of the image condition ($E_z(x = X_b)$ is even across the boundary), the result is given by

$$\mathcal{B}_I[E_z(x = X_b),\ H_x(x = X_b)] = \frac{\partial}{c_0\partial t}E_z(x = X_b) + \alpha\mu c_0\frac{\partial}{\partial y}H_x(x = X_b) \quad (10)$$

where the notation $\mathcal{B}_I$ represents the result of the integration of (9) with respect to time.

Normally (10) is set equal to zero to provide the equation used to absorb waves at the boundary. However, in the image boundary method, it is used in the equation of images (8). To see how this is accomplished examine the wave equation

$$\left(\frac{\partial^2}{c_0^2\partial t^2} - \nabla^2\right) E_z + \mu\frac{\partial}{\partial t}(\sigma E_z) = 0 \quad (11)$$

To implement the image boundary method σ is interpreted as an operator on E_z such that $\partial(\sigma E_z)/\partial t = \mathcal{B}_I[E_z(x = X_b),\ H_x(x = X_b)]$ at the boundaries. Since we assume that the fields are initially zero, we can take the integral with respect to time once more. The final result for the "loss" needed to implement the image boundary method is given by

$$\sigma E_z(x = X_b) = \frac{2}{\eta\Delta r}E_z(x = X_b) + \frac{2\alpha c_o}{\Delta r}\int_{-\infty}^{t}\frac{\partial}{\partial y}H_x(x = X_b)\,dt \quad (12)$$

For the left boundary the result is identical. Top and bottom boundary conditions are found in a similar manner. The corner conditions are found using the first-order, one-way wave equation operator. The resulting "loss" expression for all corners is given by

$$\sigma_{(\text{corner})}\, E_z = \frac{4}{\mu c_0\Delta r}E_z \quad (13)$$

The performance of the image-based boundary method is similar to that of the second-order, one-way wave equation operator [15, 20]. For our work, $\alpha = 0.6$ provided acceptable absorption over a wide range of incident angles.

V. Two-Dimensional, Free-Space Transient Results

To compare the Yee, 2-4, and 2-6 methods we use the following simulation. An 80λ-by-80λ grid is discretized at 15 PPW for a frequency of 3 MHz in free space. A Gaussian pulse point source is placed near the left edge of the computational grid. This pulse has a half-power bandwidth of 5.9 MHz. The initial time for these simulations and the introduction of the pulse occurs at $t = -\sqrt{10}\sigma$ where σ^2 is the variance of the Gaussian pulse.

For the 2-4 and 2-6 methods, since grid anisotropy is small, the speed of the medium is adjusted to make the ratio of the phase velocity to the speed of the medium unity ($c_p/c_0 = 1.0$) at a frequency of 3 MHz (this frequency was chosen for the CW scattering case discussed below) with the discretization set at 15 PPW. This is accomplished by multiplying the differencing coefficients by the average c_o/c_p computed over propagation angles from 0° to 45° in steps of 1°. For the 2-6 method the correction is $\overline{c_0/c_p} = 0.998175337$; for the 2-4 method the correction is $\overline{c_0/c_p} = 0.998241986$. The uncorrected 2-4 method has a maximum $c_p/c_0 = 1.001794346$ and a minimum $c_p/c_0 = 1.001687929$ and the uncorrected 2-6 method has a maximum $c_p/c_0 = 1.001829583$ and a minimum $c_p/c_0 = 1.00182639$. No correction was attempted for the YA because a correction would amplify the YA anisotropy. The correction for the YA would be $\overline{c_0/c_p} = 1.003710175$. The maximum and minimum uncorrected normalized phase velocities for the YA are $c_p/c_0 = 0.9981548$ and $c_p/c_0 = 0.9944013$, respectively.

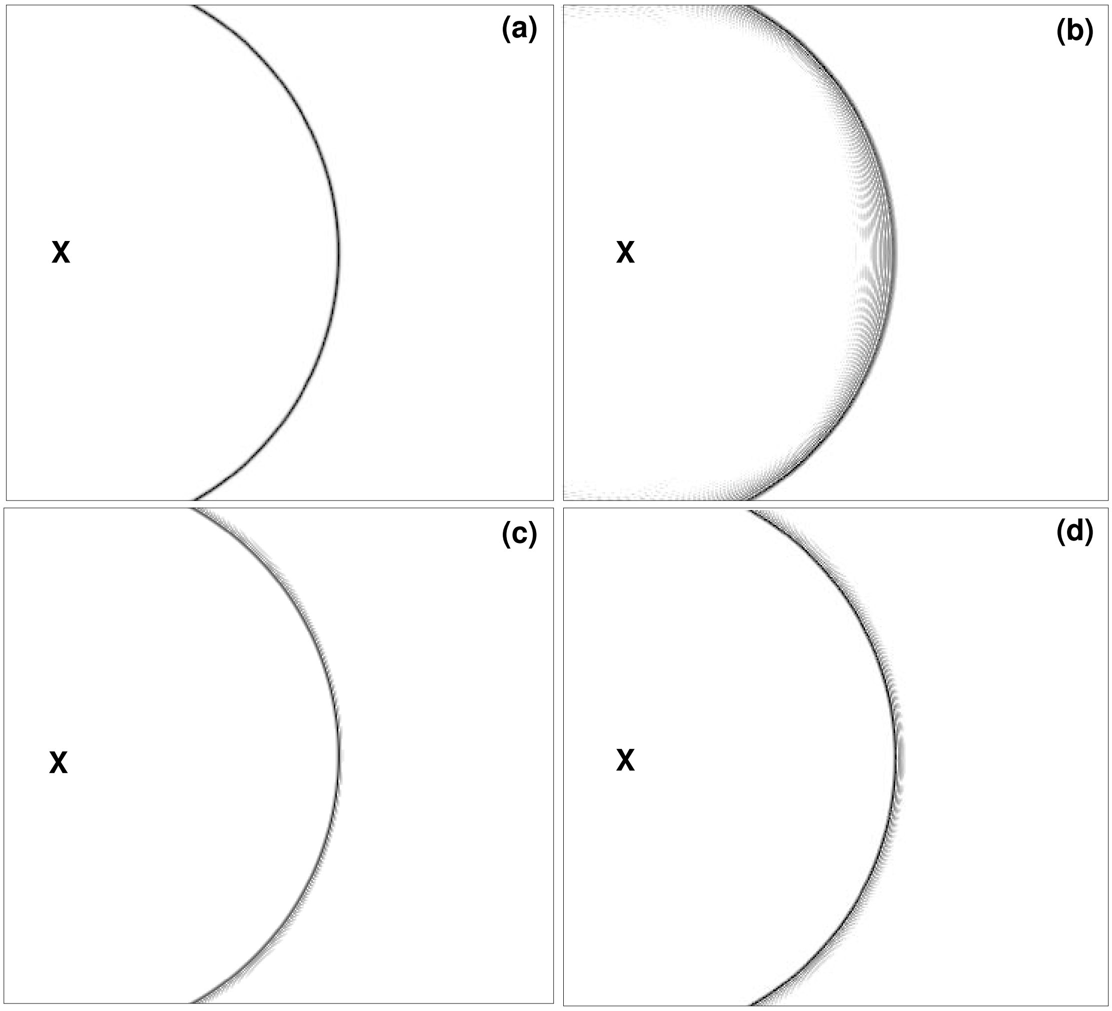

Figure 4: Two-dimensional, free-space transient pulse simulation after 1800 time iterations. Diagram 4a is the desired result, 4b is the YA result, 4c is the 2-4 result, and 4d is the 2-6 result. The magnitude of the wave is represented in greyscale with dark corresponding to the highest magnitude. Source location is indicated with an "X."

The results are shown in Fig. 4. Each snapshot is taken 240 time steps after the introduction of the pulse into the FDTD grid. In these figures the magnitude of the electric field is displayed, with the dark areas representing the highest amplitudes. The location of the source is indicated by an "X."

To quantify the error between the desired result and the simulation result a Transient Energy Difference Ratio (TEDR) is defined as

$$\mathrm{TEDR}(t) = \int_s (E_s(r,t) - E_t(r,t))^2\, ds \Big/ \int_s (E_t(r,t))^2\, ds \tag{14}$$

where $E_s(r,t)$ is the simulation result, $E_t(r,t)$ is the exact result, and the surface integral is taken over the simulation area. Note that as defined, the TEDR is a function of time and can be used to compare the accuracy of the simulation algorithms at a given time.

The exact result is shown in Fig. 4a. In Fig. 4b, calculated using the YA, the pulse has traveled approximately 8 wavelengths, at 3 MHz, and obviously differs from the exact result. Dispersion causes the higher frequency content of the pulse to travel more slowly. The maximum pulse broadening occurs along the grid lines while the minimum broadening occurs at $\pm 45°$ and $\pm 135°$ with respect to the x axis. The TEDR for the YA is 1.43.

The 2-4 result is shown in Fig. 4c. The simulation parameters are the same as for the Yee method. Although there is a slight amount of pulse broadening at $\pm 45°$ and $\pm 135°$, there is clear improvement over the YA. In this case the TEDR is 0.586. Broadening is evident prior to the pulse peak because the propagation speed increases as the frequency increases.

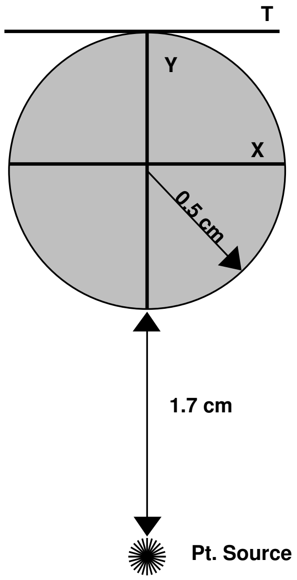

Figure 5: Geometry for scattering from a 0.5 cm radius cylinder. The line denoted by "T" represents where the results are recorded (tangent line).

In Fig. 4d the result from the 2-6 method is shown. The amount of pulse broadening is similar to the maximum broadening for the 2-4 result. Because of the decrease in grid anisotropy, however, it is nearly constant over all propagation angles. As with the 2-4 method the broadening occurs prior to the peak. In this case the TEDR is 0.869; this is larger than for the 2-4 method and is caused by a slightly larger spread of energy over time due to the larger phase error per wavelength.

VI. Scattering Results

To further evaluate the performance of the YA, 2-4, and 2-6 methods we examine a two-dimensional steady state problem in the presence of a scatterer. The problem is discretized at 15 PPW for a frequency of 3 MHz in free space. The background material is composed of a lossless material with $\epsilon = 4.444 \times 10^{-10}$ F/m and $\mu = 1000.0$ H/m. A cylinder is centered at the origin of the coordinate system as shown in Fig. 5. The radius of the cylinder is 0.5 cm. This corresponds to a radius of 10λ in the background material at 3 MHz. The cylinder is composed of a material with $\epsilon = 5.13746 \times 10^{-10}$ F/m, $\mu = 940.0$ H/m, and $\sigma = 3.72796 \times 10^{-5}$ S/m. A harmonic source with a frequency of 3 MHz is placed on the y axis at $y = -2.2$ cm.

It can be shown that the electric field for a TM-mode wave is equivalent to the acoustic pressure [21]. Thus, our problem is analogous to an acoustics problem for a fat-like cylinder in water which is of interest in ultrasound applications for biological materials. To convert between acoustic material parameters and electromagnetic parameters set $\epsilon = 1/\rho v^2$ and $\mu = \rho$ where ρ is the density of the material and v is the speed of sound in the medium. In water $v = 1490$ m/s and $\rho = 1$ g/cm^3. The cylinder has $v = 1434$ m/s, $\rho = 0.94$ g/cm^3, and an attenuation of $\alpha = 25.213$ 1/m [23].

All fields are assumed to be zero prior to the excitation of the line source. When the fields reach steady state, the magnitude and phase are measured along a line tangent to the cylinder but on the opposite side of the cylinder from the source (see Fig. 5). The results for the various methods are compared to those using a FFT-Conjugate-Gradient moment method (FFT-CG) [24, 25]. The magnitude is shown in Fig. 6 while the phase is shown in Fig. 7. Because the results are symmetric about $x = 0$, only the results for $x > 0$ are presented.

To check the accuracy of each of the simulation methods a Steady State Energy Difference Ratio is used. Similar to the TEDR but taking into account the steady state excitation, the SEDR is defined as

$$\mathrm{SEDR} = \int_l |\hat{E}_s(r) - \hat{E}_t(r)|^2 \, dl \Big/ \int_l |\hat{E}_t(r)|^2 \, dl \qquad (15)$$

where in this case $\hat{E}_s$ is the complex electric phasor from the simulation, $\hat{E}_t$ is the complex result from the FFT-CG, and the line integral is taken along the tangent line. For the YA the SEDR is 1.2468, while for the 2-4 method the SEDR is 0.1279, and for the 2-6 method the SEDR is 0.1455. Overall the 2-4 method provides the best accuracy with the 2-6 method nearly as accurate. The YA is not as accurate and from Figures 6 and 7 it can be seen that the phase errors are the most substantial. The 2-6 method is slightly less accurate than the 2-4 due to the slightly larger phase errors inherent in the 2-6 method. However, for the magnitude response there are areas in which the YA is more accurate ($|x| > 0.4$ cm). To understand this consider the magnitude and phase errors for each of the simulations.

For the magnitude, the higher-order methods provide better agreement with the FFT-CG result than the YA. The mean-square error for the magnitude is 0.103% for the YA, 0.078% for the 2-4 method, and 0.090% for the 2-6 method. For the phase, the higher-order methods are much more accurate than the YA. The mean-square error for the phase is 54.70% for the YA, 0.49% for the 2-4 method, and 0.65% for the 2-6 method. The higher-order methods are more accurate near $x = 0$ and less accurate elsewhere. For $|x| > 0.4$ cm radiation from the creeping waves propagating along the interface between the background and the scattering cylinder contributes a significant portion of the scattered field.

That the magnitude response for the higher-order methods is less accurate where the creeping wave radiation is significant is attributed to the domain over which

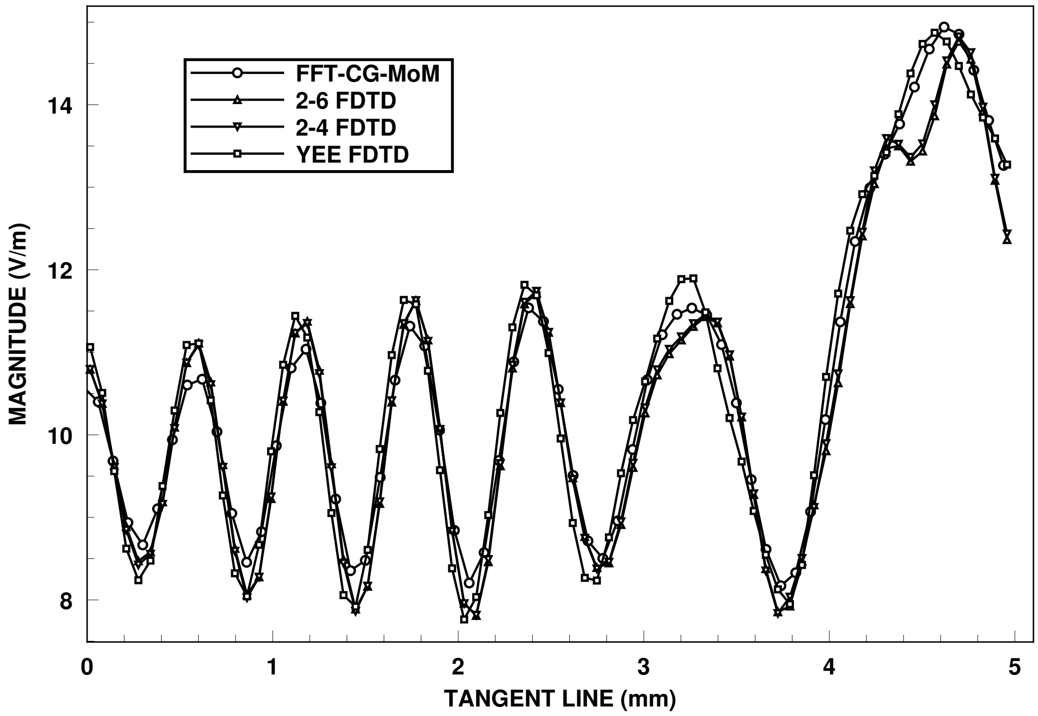

Figure 6: Magnitude versus distance along the tangent line for the YA, the 2-4 method, the 2-6 method, and the FFT-Conjugate-Gradient moment method.

the derivative is calculated. In all the simulations the discretization of the problem is identical; only the size of the spatial stencil used in calculating the derivatives changes. This spatial stencil is two points for the YA compared to either four or six points for the higher-order methods. Thus, at a material boundary the interaction between the boundary and the spatial derivative stencil are larger for the higher-order methods than for the YA. Errors caused by this interaction are largest for a guided wave, such as a creeping wave. Also from our experience with transient simulations, reflections from the boundary conditions cannot account for the error in the higher-order methods for $|x| > 0.4$ cm. Thus, we assume that the inaccuracy in this region is due to the increased spatial stencil required in simulating the creeping wave on the surface of the cylinder. Two recent papers discuss the impact of stair-step approximations for perfect conductors using the YA; however, they do not address dielectric boundaries [26, 27]. Further study is needed to examine and understand the role of increased spatial stencils used in higher-order methods and for dielectric material boundaries.

VII. Conclusions

Finite-Difference Time-Domain algorithms are inherently dispersive and anisotropic. For the Yee Algorithm (YA) errors due to numerical dispersion and anisotropy can be significant. In a large problem, 40 wavelengths and larger, phase errors can quickly exceed $\pi/8$. Phase errors can be reduced at the expense of finer discretization. However, fine discretization leads to prohibitive memory requirements and high computational cost due to the large number of points that must be computed and stored.

To reduce the resource requirements, higher-order approximations were used for the spatial derivatives in Maxwell's curl equations. Two higher-order algorithms were developed, one fourth-order in space and second-order in time and the other sixth-order in space and second-order in time. These algorithms reduced both numerical dispersion and grid anisotropy, permitting a smaller number of points per wavelength to be used and thus saving computer memory and reducing the total number of operations needed. The edges of the computational domain were treated using an image-based absorbing boundary condition.

Both transient and CW simulations were performed to compare the accuracy of the YA and higher-order methods at a fixed discretization. This was done to demonstrate the improved accuracy that can be obtained when using a higher-order method. A two-dimensional pulse in free space demonstrated the effect of dispersion and grid anisotropy for the various algorithms. The effects of grid anisotropy and dispersion were clearly evident for the YA, while they were greatly reduced using the higher-

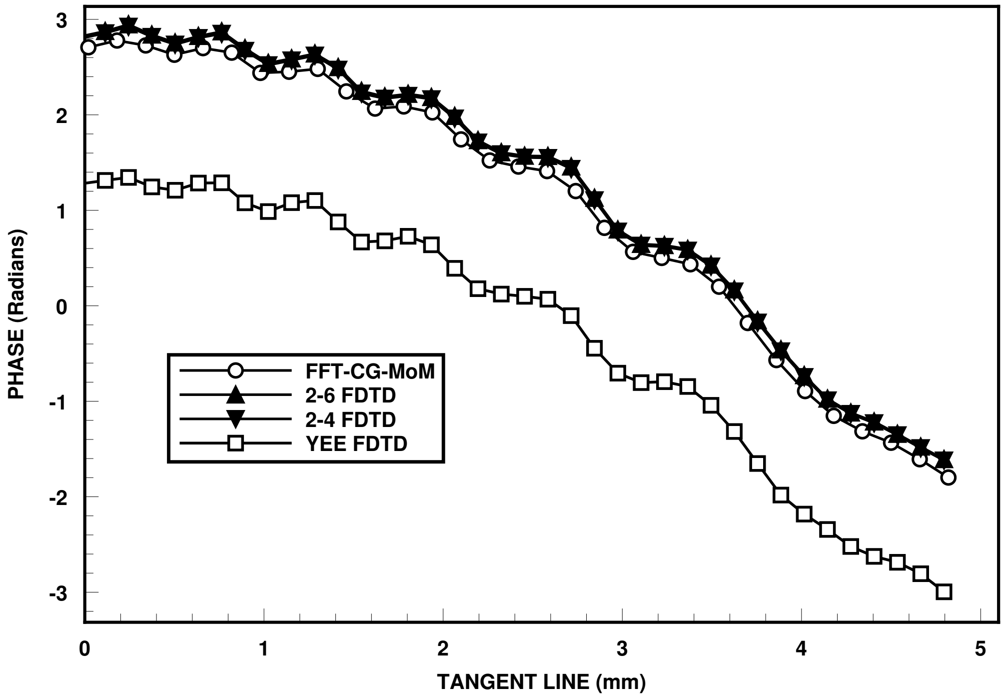

Figure 7: Phase versus distance along the tangent line for the YA, the 2-4 method, the 2-6 method, and the FFT-Conjugate-Gradient moment method.

order methods. Based on transient and steady state energy difference ratios (TEDR and SEDR) the 2-4 method is more than twice as accurate while the 2-6 method is approximately 1.65 times as accurate as the YA for the test cases examined in this paper. Simulations involving a large, weak scattering cylinder illuminated by a harmonic line source were performed. The higher-order methods were approximately an order of magnitude more accurate than the YA. However, the higher-order methods were less accurate in magnitude response when radiation from creeping, or guided, waves was a significant part of the scattered field. More work is required to fully understand the interaction of material interfaces with the increased spatial stencil used in the higher-order methods.

Acknowledgments

The authors would like to thank Karl Hakimian of the School of Electrical Engineering and Computer Science, Washington State University, and Gregory Bell of Information Systems, Washington State University, for their help in optimizing the code used in this work. We would also like to thank Dr. Robert Bamberger of the School of Electrical Engineering and Computer Science, Washington State University for the use of the S.P.I.F. lab used in preparing the figures in the paper. This work was supported by the San Diego Supercomputer Center where all simulations were performed and by the National Science Foundation under grant No. ECS-9253547.

References

[1] K. S. Yee, "Numerical Solution of Initial Boundary Value Problems Involving Maxwell's Equations in Isotropic Media," *IEEE Trans. Antennas Propagat.*, Vol. 14, 302-307 (1966).

[2] A. Taflove, "Review of the Formulation and Applications of the Finite-Difference Time-Domain Method of Numerical Modeling of Electromagnetic Wave Interactions with Arbitrary Structures," *Wave Motion*, Vol. 10, 547-582 (1988).

[3] A. Taflove and M. E. Brodwin, "Numerical Solution of Steady-State Electromagnetic Scattering Problems Using the Time-Dependent Maxwell's Equations," *IEEE Trans. Microwave Theory Tech.*, Vol. 23, No. 8, 623-630 (1975).

[4] J. Vidale, D. V. Helmberger, and R. W. Clayton, "Finite-Difference Seismograms for SH Waves," *Bull. Seism. Soc. Am.*, Vol. 75, No. 6, 1765-1782 (1985).

[5] M. A. Dablain, "The Application of High-Order Differencing to the Scalar Wave Equation," *Geophysics*, Vol. 51, No. 1, 54-66 (1986).

[6] A. Bayliss, K. E. Jordan, B. J. LeMesurier, and E. Turkel, "A Fourth-Order Accurate Finite-Difference Scheme for the Computation of Elastic Waves," *Bull. Seism. Soc. Am.*, Vol. 76, No. 4, 1115-1132 (1986).

[7] A. R. Levander, "Fourth-Order Finite-Difference P-SV Seismograms," *Geophysics*, Vol. 53, No. 11, 1425-1426 (1988).

[8] J. Fang, "Time Domain Finite Difference Computation for Maxwell's Equations," PhD. Dissertation, University of California at Berkeley, 1989, chapter 5.

[9] T. Deveze, L. Beaulieu, and W. Tabbara, "A Fourth-Order Scheme for the FDTD Algorithm Applied to Maxwell's Equations," *IEEE AP-S Symposium Chicago*, 346-349 (1992).

[10] M. Abromowitz and I. A. Stegun, Eds., *Handbook of Mathematical Functions,* New York: Dover Publishing, 1972, Chapter 25.

[11] K. L. Shlager, J. G. Maloney, S. L. Ray, and A. F. Peterson, "Relative Accuracy of Several Finite-Difference Time-Domain Methods in Two and Three Dimensions," *IEEE Trans. Antennas Propagat.,* Vol. 41, No. 12, 1732-1737 (1993).

[12] P. G. Petropoulos, "Phase Error Control for FDTD Methods of Second and Fourth Order Accuracy," *IEEE Trans. Antennas Propagat.,* Vol. 42, No. 6, 859-862 (1994)

[13] B. Engquist and A. Majda, "Absorbing Boundary Conditions for the Numerical Simulation of Waves," *Math. Comput.,* Vol. 31, 629-651 (1977).

[14] G. Mur, "Absorbing Boundary Conditions for the Finite-Difference Approximation of Time-Domain Electromagnetic Field Equations," *Trans. Electromagn. Compat.,* Vol. EMC-23, 377-382 (1981).

[15] T. G. Moore, J. G. Blaschak, A. Taflove, and G. A. Kriegsmann, "Theory and Application of Radiation Boundary Operators," *IEEE Trans. Antennas Propagat.,* Vol. 36, No. 12, 1797-1812 (1988).

[16] A. R. Levander, "Use of Telegraphy Equation to Improve Absorbing Boundary Efficiency for Fourth-Order Acoustic Wave Finite Difference Schemes," *Bull. Seismol. Soc. Am.,* Vol. 75, No. 6, 1847-1852.

[17] Z. P. Liao, H. L. Wong, B. P. Yang, and Y. F. Yuan, "A Transmitting Boundary for Transient Wave Analyses," *Scientia Sinica*, series A, Vol. 17, No. 10, 1063-1076 (1984).

[18] T. Deveze, L. Beaulieu, and W. Tabbara, "An Absorbing Boundary Condition for the Fourth-Order FDTD Scheme," *IEEE AP-S Symposium Chicago*, 342-345 (1992).

[19] K. K. Mei, J. Fang, "Superabsorption–A Method to Improve Absorbing Boundary Conditions," *IEEE Trans. Microwave Theory Tech.,* Vol. 40, No. 9, 1001-1010 (1992).

[20] T. Deveze, F. Clerc, and W. Tabbara, "Second Order Pseudo-Transparent Boundary Equations for FDTD Method," *IEEE AP-S Symposium Dallas*, 1624-1627 (1990).

[21] J. J. Bowman, T. B. A. Senior, and P. L. E. Uslenghi, Eds., *Electromagnetic and Acoustic Scattering by Simple Shapes*, New York: Hemisphere Publishing, 1987, Chapter 1.

[22] P.N.T. Wells, *Biomedical Ultrasonics*, New York: Academic Press, 1977, Chapter 1.

[23] E. L. Madsen, J. A. Zagzebski, G. R. Frank, J. F. Greenleaf, and P. L. Carson, "Anthropomorphic Breast Phantoms for Assessing Ultrasonic Imaging System Performance and for Training Ultrasonographers: Part II," *J. Clin. Ultrasound*, Vol. 10, 91-100 (1982).

[24] D. T. Borup and O. P. Gandhi, "Calculation of High-Resolution SAR Distributions in Biological Bodies Using the FFT Algorithm and Conjugate Gradient Method," *IEEE Trans. Microwave Theory Tech.,* Vol. 33, No. 5, 417-419 (1985).

[25] T. K. Sarkar and E. Arvas, "On a Class of Finite Step Iterative Methods (Conjugate Directions) for the Solution of an Operator Equation Arising in Electromagnetics," *IEEE Trans. Antennas Propagat.,* Vol. 33, No. 10, 1058-1066 (1985).

[26] A. C. Cangellaris and D. B. Wright, "Analysis of the Numerical Error Caused by the Stair-Stepped Approximation of a Conducting Boundary in FDTD Simulations of Electromagnetic Phenomena," *IEEE Trans. Antennas Propagat.,* Vol. 39, No. 10, 1518-1525 (1991)

[27] R. Holland, "Pitfalls of Staircase Meshing", *IEEE Trans. Electromagn. Compat.,* Vol. 35, No. 4, 434-439 (1993)

[28] A. Taflove, "Advanced Numerical Modeling of Microwave Penetration and Coupling for Complex Structures–Final Report," Lawrence Livermore National Laboratory, Sept. 1987 under Contract No. 6599805, UCRL-15960

Appendix A: Stability Analysis

The stability analysis presented here is an extension of the analysis reported by Taflove and is based on the Courant, Friedrich, and Levy (CFL) and von Neumann methods [28]. Waves are decomposed into Fourier eigenmodes and their eigenvalues are examined to find the relation between Δt, Δx and Δy that guarantees stability. The FDTD difference equations are examined using a separate analysis for the stability for the temporal derivative approximation and the spatial derivative approximations. The analysis for the temporal derivative approximation provides the upper bound for the eigenvalue for stable eigenmodes. The spatial analysis provides the bounds for the spectrum of plane wave eigenmodes. Then by requiring the complete spectrum of eigenmodes to be contained within the stable range, all possible wave modes will be stable.

Without loss of generality, TM mode waves are assumed to propagate in a homogeneous medium. The equations of motion are

$$\frac{\partial E_z}{\partial t} = \frac{1}{\epsilon} \cdot \left(\frac{\partial H_y}{\partial x} - \frac{\partial H_x}{\partial y} \right) \tag{16}$$

$$\frac{\partial H_x}{\partial t} = -\frac{1}{\mu} \cdot \frac{\partial E_z}{\partial y} \tag{17}$$

$$\frac{\partial H_y}{\partial t} = \frac{1}{\mu} \cdot \frac{\partial E_z}{\partial x} \tag{18}$$

From the work by Taflove the time eigenvalue problem gives the requirement for stability due to time-differentiation alone. Taflove shows that the eigenvalue is purely imaginary and must be bound for stability by [28]

$$\mid \mathrm{Imag}(\Lambda) \mid \leq \frac{2}{\Delta t} \tag{19}$$

where Λ is an eigenvalue. Since all the algorithms considered in this paper use second-order time differences this bound is required for the YA, 2-4, and 2-6 methods.

However, spatial stability requirements are different for each of the three algorithms. To start, isolate the right-hand side of (16) through (18) as an eigenvalue problem and replace the spatial derivatives with the difference equations.

$$\begin{aligned}\Lambda\epsilon E_z(i,j) = {} & [d_3 H_y(i+5/2,j) + d_2 H_y(i+3/2,j) \\ & + d_1 H_y(i+1/2,j) - d_1 H_y(i-1/2,j) \\ & - d_2 H_y(i-3/2,j) - d_3 H_y(i-5/2,j)]/\Delta x \\ & - [d_3 H_x(i,j+5/2) + d_2 H_x(i,j+3/2) \\ & + d_1 H_x(i,j+1/2) - d_1 H_x(i,j-1/2) \\ & - d_2 H_x(i,j-3/2) - d_3 H_x(i,j-5/2)]/\Delta y\end{aligned} \tag{20}$$

$$\begin{aligned}\Lambda\mu H_x(i,j) = {} & \\ -[& d_3 E_z(i,j+5/2) + d_2 E_z(i,j+3/2) \\ & + d_1 E_z(i,j+1/2) - d_1 E_z(i,j-1/2) \\ & - d_2 E_z(i,j-3/2) - d_3 E_z(i,j-5/2)]/\Delta y\end{aligned} \tag{21}$$

$$\begin{aligned}\Lambda\mu H_y(i,j) = {} & \\ [& d_3 E_z(i+5/2,j) + d_2 E_z(i+3/2,j) \\ & + d_1 E_z(i+1/2,j) - d_1 E_z(i-1/2,j) \\ & - d_2 E_z(i-3/2,j) - d_3 E_z(i-5/2,j)]/\Delta x\end{aligned} \tag{22}$$

where E_z, H_x, and H_y are the eigenmodes with eigenvalue Λ, $E_z(i,j) = E_z(i \cdot \Delta x, j \cdot \Delta y)$ with the magnetic field components having a similar interpretation, and for the various methods

Yee's Method (2-2):	$d_1 = 1$
	$d_2 = 0$
	$d_3 = 0$
2-4 Method:	$d_1 = 36/24$
	$d_2 = -1/24$
	$d_3 = 0$
2-6 Method:	$d_1 = 2250/1920$
	$d_2 = -125/1920$
	$d_3 = 9/1920$

Now, assume that the eigenmodes are TM plane waves propagating in two dimensions

$$E_z(i,j) = E_{zo} e^{\imath(\tilde{k}_x i \Delta x + \tilde{k}_y j \Delta y)} \tag{23}$$

$$H_x(i,j) = H_{xo} e^{\imath(\tilde{k}_x i \Delta x + \tilde{k}_y j \Delta y)} \tag{24}$$

$$H_y(i,j) = H_{yo} e^{\imath(\tilde{k}_x i \Delta x + \tilde{k}_y j \Delta y)} \tag{25}$$

where E_{zo}, H_{xo}, H_{yo} are the amplitudes of the components of the propagating waves, $\tilde{k}_x$ and $\tilde{k}_y$ are the x and y components of the Fourier wave vector, and $\imath = \sqrt{-1}$. Using this expansion, stability for any wave can be examined since any wave can be decomposed into its temporal and spatial representation.

Taking the above eigenmodes and substituting them into (20) through (22), using Euler's formula, and removing common terms, yields

$$H_{xo} = -E_{zo} \cdot \frac{2\imath}{\Lambda\mu\Delta y} [d_3 \sin(5A_y) + d_2 \sin(3A_y) + d_1 \sin(A_y)] \tag{26}$$

$$H_{yo} = E_{zo} \cdot \frac{2\imath}{\Lambda\mu\Delta x} [d_3 \sin(5A_x) + d_2 \sin(3A_x) + d_1 \sin(A_x)] \tag{27}$$

$$E_{zo} = \frac{2\imath}{\Lambda\epsilon} \cdot \left\{ \frac{H_{yo}}{\Delta x}[d_3 \sin(5A_x) + d_2 \sin(3A_x) + d_1 \sin(A_x)] - \frac{H_{xo}}{\Delta y}[d_3 \sin(5A_y) + d_2 \sin(3A_y) + d_1 \sin(A_y)] \right\} \quad (28)$$

where $A_x = \tilde{k}_x \Delta x/2$ and $A_y = \tilde{k}_y \Delta y/2$. Then substituting (26) and (27) into (28) and solving for Λ gives

$$\Lambda^2 = \frac{-4}{\mu\epsilon} \cdot (Z_x/\Delta x^2 + Z_y/\Delta y^2) \quad (29)$$

where

$$Z_x = [d_3 \sin(5A_x) + d_2 \sin(3A_x) + d_1 \sin(A_x)]^2 \quad (30)$$

$$Z_y = [d_3 \sin(5A_y) + d_2 \sin(3A_y) + d_1 \sin(A_y)]^2 \quad (31)$$

To examine the bounds on Λ, expand Z_x and use trigonometric identities for $\sin(3A_x)$ and $\sin(5A_x)$ to obtain an expression containing only even powers of $\sin(A_x)$, $\sin(3A_x)$, and $\sin(5A_x)$ (a similar approach is used for Z_y). The result is

$$\begin{aligned} Z_x &= d_3^2 \sin^2(5A_x) + d_2^2 \sin^2(3A_x) \\ &+ d_1^2 \sin^2(A_x) + 2d_1d_2[3\sin^2(A_x) - 4\sin^4(A_x)] \\ &+ 2d_1d_3[5\sin^2(A_x) - 20\sin^4(A_x) + 16\sin^6(A_x)] \\ &+ 2d_2d_3[15\sin^2(A_x) - 80\sin^4(A_x) \\ &+ 128\sin^6(A_x) - 64\sin^2(A_x)] \end{aligned} \quad (32)$$

Clearly, all the even powers of $\sin(A_x)$, $\sin(3A_x)$, and $\sin(5A_x)$ are between 0 and 1. Thus the upper bound for both Z_x and Z_y are found using the appropriate values for d_1, d_2, and d_3 for each method (YA, 2-4, and 2-6). The results are

Yee's Method (2-2):	$\text{Max}(Z) = 1$
2-4 Method:	$\text{Max}(Z) = 49/36$
2-6 Method:	$\text{Max}(Z) = 22201/14400$

where $\text{Max}(Z) = \text{Max}(Z_x) = \text{Max}(Z_y)$.

From (29) Λ is purely imaginary and the bounds on Λ are given by

Yee's Method (2-2):

$$|\ \text{Imag}(\Lambda)\ | \leq 2c \cdot \left(\frac{1}{\Delta x^2} + \frac{1}{\Delta y^2}\right)^{1/2} \quad (33)$$

2-4 Method:

$$|\ \text{Imag}(\Lambda)\ | \leq 2c \cdot \frac{7}{6} \cdot \left(\frac{1}{\Delta x^2} + \frac{1}{\Delta y^2}\right)^{1/2} \quad (34)$$

2-6 Method:

$$|\ \text{Imag}(\Lambda)\ | \leq 2c \cdot \frac{149}{120} \cdot \left(\frac{1}{\Delta x^2} + \frac{1}{\Delta y^2}\right)^{1/2} \quad (35)$$

To *guarantee* stability for an arbitrary eigenmode, the eigenvalues must be contained completely within the bounds for the spatial modes and the time stepping bounds. Thus combining the spatial bounds with the bound from the time-differencing, the stability limit for each of the algorithms (setting $\Delta x = \Delta y = h$) is

Yee's Method (2-2):

$$\Delta t \leq \frac{h}{c\sqrt{2}} \quad (36)$$

2-4 Method:

$$\Delta t \leq \frac{6}{7} \cdot \frac{h}{c\sqrt{2}} \quad (37)$$

2-6 Method:

$$\Delta t \leq \frac{120}{149} \cdot \frac{h}{c\sqrt{2}} \quad (38)$$

The requirement for Yee's algorithm is well known. The result for the 2-4 method agrees with the calculation by Fang [8].

Appendix B: Calculating Dispersion Curves

In this appendix the dispersion equations for the various methods are presented. This analysis is an extension of the method first reported by Taflove [28]. TM propagation is assumed. A plane wave propagating at an angle ϕ with respect to the x axis is given by

$$E_z^n(i,j) = E_{zo}\, e^{\imath(k[\cos(\phi)i\Delta x + \sin(\phi)j\Delta y] - \omega n \Delta t)} \quad (39)$$

$$H_x^n(i,j) = H_{xo}\, e^{\imath(k[\cos(\phi)i\Delta x + \sin(\phi)j\Delta y] - \omega n \Delta t)} \quad (40)$$

$$H_y^n(i,j) = H_{yo}\, e^{\imath(k[\cos(\phi)i\Delta x + \sin(\phi)j\Delta y] - \omega n \Delta t)} \quad (41)$$

where k is the wavenumber, ω is the frequency, $\imath = \sqrt{-1}$, and E_{zo}, H_{xo}, H_{yo} are the field amplitudes.

The expressions above are placed into the discretized Maxwell's equations, and amplitude terms are eliminated to obtain the following expression

$$\begin{aligned} \left(\tfrac{h}{c\Delta t}\right)^2 \sin^2\left(\tfrac{w\Delta t}{2}\right) &= \\ [d_1 \sin(\tfrac{kh}{2}\cos\phi) &+ d_2 \sin(\tfrac{3kh}{2}\cos\phi) \\ + d_3 \sin(\tfrac{5kh}{2}\cos\phi)]^2 &+ [d_1 \sin(\tfrac{kh}{2}\sin\phi) \\ + d_2 \sin(\tfrac{3kh}{2}\sin\phi) &+ d_3 \sin(\tfrac{5kh}{2}\sin\phi)]^2 \end{aligned} \quad (42)$$

where we have set $h = \Delta x = \Delta y$. Then setting the values for d_1, d_2, and d_3 (from Appendix A) for the various methods, the effective wavenumber k can be obtained numerically for a given set of h, Δt, and propagation angle ϕ. Once k is known, the effective phase velocity can be calculated.